

A CFD Model for Simulating Urban Flow and Dispersion

JONG-JIN BAIK

School of Earth and Environmental Sciences, Seoul National University, Seoul, South Korea

JAE-JIN KIM AND HARINDRA J. S. FERNANDO

Environmental Fluid Dynamics Program, Department of Mechanical and Aerospace Engineering, Arizona State University, Tempe, Arizona

(Manuscript received 5 April 2002, in final form 9 January 2003)

ABSTRACT

A three-dimensional computational fluid dynamics (CFD) model is developed to simulate urban flow and dispersion, to understand fluid dynamical processes therein, and to provide practical solutions to some emerging problems of urban air pollution. The governing equations are the Reynolds-averaged equations of momentum, mass continuity, heat, and other scalar (here, passive pollutant) under the Boussinesq approximation. The Reynolds stresses and turbulent fluxes are parameterized using the eddy diffusivity approach. The turbulent diffusivities of momentum, heat, and pollutant concentration are calculated using the prognostic equations of turbulent kinetic energy and its dissipation rate. The set of governing equations is solved numerically on a staggered, nonuniform grid system using a finite-volume method with the semi-implicit method for pressure-linked equation (SIMPLE) algorithm. The CFD model is tested for three different building configurations: infinitely long canyon, long canyon of finite length, and orthogonally intersecting canyons. In each case, the CFD model is shown to simulate urban street-canyon flow and pollutant dispersion well.

1. Introduction

The urban roughness sublayer is at the bottom of the urban boundary layer, and its characteristics are mechanically and thermally affected by roughness elements such as buildings, structures, trees, vehicles, and so on (Raupach et al. 1991; Roth 2000). The urban roughness sublayer extends from the surface up to a height of 2–5 times the height of roughness elements (Rotach 1995). The flow therein is strongly influenced by local meteorological conditions and surrounding or underlying roughness elements. For example, a strong shear layer is created near the top of buildings, generating high levels of turbulence. There are numerous sources of pollutants in urban areas. Some of them are sustained (emissions from motor vehicles), and others result from accidental releases of significant amounts. The nature of flow and turbulence in the urban roughness sublayer greatly affects the transport of those contaminants.

Flow and dispersion in urban areas have been extensively studied during the past two decades. These include physical modeling (wind tunnel or water tank; e.g., Hoydysh and Dabberdt 1988; Meroney et al. 1996;

Uehara et al. 2000; Baik et al. 2000; Brown et al. 2001), numerical modeling (e.g., Lee and Park 1994; Sini et al. 1996; Baik and Kim 1999), and observational (e.g., DePaul and Sheih 1985, 1986; Nakamura and Oke 1988; Rotach 1995) studies. With ever-increasing computing power, computational fluid dynamics (CFD) models have become an important tool in urban flow and dispersion research. It is now possible with state-of-the-art computers to simulate building-scale flow and dispersion in a real urban setting (Lee et al. 2001).

We have developed a three-dimensional CFD model that can be effectively used for basic research as well as practical applications. This paper describes our CFD model and presents some simulation results. The CFD model to be presented here extends and improves our previous two-dimensional street-canyon model (Baik and Kim 1999; Kim and Baik 1999). Section 2 describes the basic framework of the three-dimensional CFD model, which is applied to simulate urban flow and dispersion in section 3. The summary and conclusions are given in section 4.

2. Model description

a. Governing equations

Under the Boussinesq approximation and large Rossby numbers (i.e., negligible Coriolis effects), the Reyn-

Corresponding author address: Jong-Jin Baik, School of Earth and Environmental Sciences, Seoul National University, Seoul 151-742, South Korea.
E-mail: jjbaik@snu.ac.kr

olds-averaged equations of momentum, mass continuity, heat, and other scalar can be expressed as (Zhang et al. 1996; Arya 1999)

$$\frac{\partial U_i}{\partial t} + U_j \frac{\partial U_i}{\partial x_j} = -\frac{1}{\rho_0} \frac{\partial P^*}{\partial x_i} + \delta_{ij} g \frac{T^*}{T_0} + \nu \frac{\partial^2 U_i}{\partial x_j \partial x_j} - \frac{\partial}{\partial x_j} (\overline{u_i u_j}), \quad (1)$$

$$\frac{\partial U_j}{\partial x_j} = 0, \quad (2)$$

$$\frac{\partial T}{\partial t} + U_j \frac{\partial T}{\partial x_j} = \kappa \frac{\partial^2 T}{\partial x_j \partial x_j} - \frac{\partial}{\partial x_j} (\overline{T' u_j}) + S_h, \quad \text{and} \quad (3)$$

$$\frac{\partial C}{\partial t} + U_j \frac{\partial C}{\partial x_j} = D \frac{\partial^2 C}{\partial x_j \partial x_j} - \frac{\partial}{\partial x_j} (\overline{c u_j}) + S_c. \quad (4)$$

Here, t is the time, x_i is the i th Cartesian coordinate, U_i is the i th mean velocity component, P^* is the deviation of pressure from its reference value, T is the mean temperature, and C is the mean concentration of species in air (say, pollutant); u_i , T' , and c are the fluctuations from their respective means U_i , T , and C , respectively; and ρ_0 is the air density, T_0 is the reference temperature, T^* is the deviation of temperature from its reference value ($=T - T_0$), δ_{ij} is the Kronecker delta, and g is the gravitational acceleration. In (1), ν is the kinematic viscosity of air, κ in (3) is the thermal diffusivity, and D in (4) is the molecular diffusivity of pollutant. Respectively, S_h in (3) and S_c in (4) denote the source/sink terms of heat and pollutant. Pollutant is assumed to be inert and neutrally buoyant. Differentiating (1) with respect to x_i and using (2) gives a Poisson equation for P^* , from which P^* is diagnostically calculated.

b. Turbulence closure model

To close the above-mentioned set of governing equations, the Reynolds stresses and turbulent fluxes in (1), (3), and (4) should be parameterized in terms of grid-resolvable variables. In the CFD model, these are parameterized using the eddy diffusivity approach (Sini et al. 1996):

$$-\overline{u_i u_j} = K_m \left(\frac{\partial U_i}{\partial x_j} + \frac{\partial U_j}{\partial x_i} \right) - \frac{2}{3} \delta_{ij} k, \quad (5)$$

$$-\overline{T' u_j} = K_h \frac{\partial T}{\partial x_j}, \quad \text{and} \quad (6)$$

$$-\overline{c u_j} = K_c \frac{\partial C}{\partial x_j}, \quad (7)$$

where K_m , K_h , and K_c are the eddy (or turbulent) diffusivities of momentum (also called the eddy viscosity), heat, and pollutant concentration, respectively, and $k = \overline{u_i u_i}/2$ is the turbulent kinetic energy. The eddy viscosity can be related to k and its dissipation rate ε by

$$K_m = C_\mu \frac{k^2}{\varepsilon}, \quad (8)$$

where C_μ is an empirical constant. Here, the effective Prandtl number Pr and Schmidt number Sc are defined as

$$Pr = \frac{\nu + K_m}{\kappa + K_h} \quad \text{and} \quad (9)$$

$$Sc = \frac{\nu + K_m}{D + K_c}. \quad (10)$$

In the model, the turbulent kinetic energy and its dissipation rate are prognostically computed using

$$\begin{aligned} \frac{\partial k}{\partial t} + U_j \frac{\partial k}{\partial x_j} = & -\overline{u_i u_j} \frac{\partial U_i}{\partial x_j} + \frac{\delta_{ij} g}{T_0} \overline{T' u_j} \\ & + \frac{\partial}{\partial x_j} \left(\frac{K_m}{\sigma_k} \frac{\partial k}{\partial x_j} \right) - \varepsilon \quad \text{and} \end{aligned} \quad (11)$$

$$\begin{aligned} \frac{\partial \varepsilon}{\partial t} + U_j \frac{\partial \varepsilon}{\partial x_j} = & -C_{\varepsilon 1} \frac{\varepsilon}{k} \overline{u_i u_j} \frac{\partial U_i}{\partial x_j} + C_{\varepsilon 1} \frac{\varepsilon}{k} \frac{\delta_{ij} g}{T_0} \overline{T' u_j} \\ & + \frac{\partial}{\partial x_j} \left(\frac{K_m}{\sigma_\varepsilon} \frac{\partial \varepsilon}{\partial x_j} \right) - C_{\varepsilon 2} \frac{\varepsilon^2}{k}, \end{aligned} \quad (12)$$

where σ_k , σ_ε , $C_{\varepsilon 1}$, and $C_{\varepsilon 2}$ are empirical constants. The first and second terms on the right-hand side of (11) represent the shear production and buoyancy production of turbulent kinetic energy, respectively. Experiments indicate that the Prandtl number and Schmidt number are roughly constant (Sini et al. 1996) in the absence of significant buoyancy effects. Thus, the effective diffusivities of heat ($\kappa + K_h$) and pollutant concentration ($D + K_c$) can be calculated using (9) and (10), respectively, with specified values of Pr and Sc . Because for high-Reynolds-number flow, $K_m \gg \nu$, $K_h \gg \kappa$, and $K_c \gg D$, the effective diffusivities are practically the eddy diffusivities. The Pr and Sc and constants in (8), (11), and (12) are specified as (Zhang et al. 1996; Kim and Baik 1999)

$$\begin{aligned} (Pr, Sc, C_\mu, \sigma_k, \sigma_\varepsilon, C_{\varepsilon 1}, C_{\varepsilon 2}) \\ = (0.7, 0.9, 0.09, 1.0, 1.3, 1.44, 1.92). \end{aligned} \quad (13)$$

c. Numerical method

The governing equation set is numerically solved on a staggered grid system using a finite-volume method with the semi-implicit method for pressure-linked equation (SIMPLE) algorithm (Patankar 1980). At each time step, three components of velocity are prognostically calculated with an assumed pressure deviation field. Then, the pressure deviation is diagnostically calculated by solving the pressure-Poisson equation, and each velocity component is adjusted with the pressure correction. This procedure is repeated until solutions converge with a desired accuracy. On the staggered grid system,

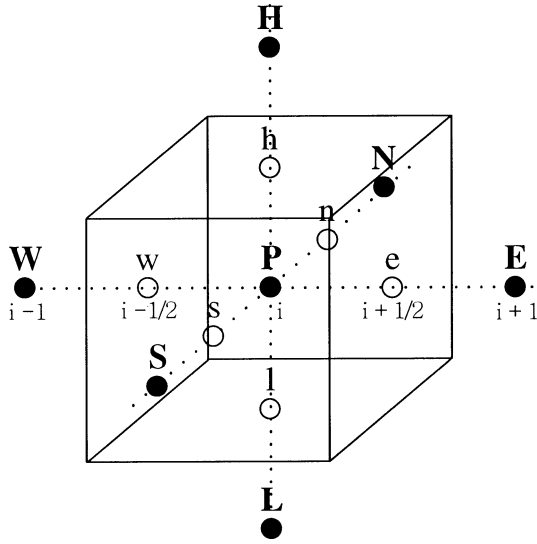


FIG. 1. A schematic of grid structure and control volume for finite differencing. The center point of the control volume is denoted by symbol P , and the other surrounding points are denoted by W , w , e , and E in the x direction; S , s , n , and N in the y direction; and L , l , h , and H in the z direction. For clarity of the figure, only grid indices in the x direction are given. In the text, the grid interval between points w and e is denoted by Δ_x^i and the grid interval between points P and E is denoted by $\Delta_{i+1/2}^x$. Intervals Δ_j^y , $\Delta_{j+1/2}^y$, Δ_k^z , and $\Delta_{k+1/2}^z$ are similarly defined.

each component of velocity (U , V , W) is defined at the center of each face of a control volume and scalar quantities (P^* , T , C , k , ε) are defined at the center of the control volume.

To illustrate the numerical procedure used to solve the equation set, the equation of pollutant concentration is taken here. Using (2), (4), and (7), the concentration equation can be written as

$$\begin{aligned} \frac{\partial}{\partial t}(\rho C) + \frac{\partial}{\partial x} \left[\rho C U - \rho(D + K_c) \frac{\partial C}{\partial x} \right] \\ + \frac{\partial}{\partial y} \left[\rho C V - \rho(D + K_c) \frac{\partial C}{\partial y} \right] \\ + \frac{\partial}{\partial z} \left[\rho C W - \rho(D + K_c) \frac{\partial C}{\partial z} \right] = \rho S_c, \end{aligned} \quad (14)$$

where ρ is used instead of ρ_0 for generality. Figure 1 shows a schematic of grid structure and control volume for finite differencing. The concentration equation [(14)] and mass continuity equation [(2)] multiplied by density can be differenced in the control volume as

$$\begin{aligned} \frac{(\rho C)_P^{n+1} - (\rho C)_P^n}{\Delta t} \Delta_x^i \Delta_j^y \Delta_k^z + (J_x|_e - J_x|_w) \Delta_j^y \Delta_k^z \\ + (J_y|_n - J_y|_s) \Delta_i^x \Delta_k^z + (J_z|_h - J_z|_l) \Delta_i^x \Delta_j^y \\ = S_p \Delta_i^x \Delta_j^y \Delta_k^z \quad \text{and} \end{aligned} \quad (15)$$

$$\begin{aligned} (F_x|_e - F_x|_w) \Delta_j^y \Delta_k^z + (F_y|_n - F_y|_s) \Delta_i^x \Delta_k^z \\ + (F_z|_h - F_z|_l) \Delta_i^x \Delta_j^y = 0, \end{aligned} \quad (16)$$

respectively. Here, $S_p = \rho S_c$, $J_x = F_x C - \mu \partial C / \partial x$, $J_y = F_y C - \mu \partial C / \partial y$, and $J_z = F_z C - \mu \partial C / \partial z$, where $F_x = \rho U$, $F_y = \rho V$, $F_z = \rho W$, and $\mu = \rho(D + K_c)$. For example, $J_x|_e$ means that J_x is evaluated at point e . The superscript n denotes the time step index and Δt is the time step. Respectively, Δ_i^x , Δ_j^y , and Δ_k^z are the grid sizes in the x , y , and z directions. Multiplying C_p in (16) and then subtracting it from (15) gives

$$\begin{aligned} \frac{(\rho C)_P^{n+1} - (\rho C)_P^n}{\Delta t} \Delta_i^x \Delta_j^y \Delta_k^z \\ + [(J_x|_e - F_x|_e C_p) - (J_x|_w - F_x|_w C_p)] \Delta_j^y \Delta_k^z \\ + [(J_y|_n - F_y|_n C_p) - (J_y|_s - F_y|_s C_p)] \Delta_i^x \Delta_k^z \\ + [(J_z|_h - F_z|_h C_p) - (J_z|_l - F_z|_l C_p)] \Delta_i^x \Delta_j^y = S_p, \end{aligned} \quad (17)$$

where the superscript $n + 1$ is omitted from the quantities in brackets and S_p for simplicity.

Following the procedure described in Patankar (1980), the exact solutions of the J terms in (17) can be derived as

$$J_e = F_e \left[C_p + \frac{C_p - C_e}{\exp(A_e) - 1} \right], \quad (18)$$

$$J_w = F_w \left[C_w + \frac{C_w - C_p}{\exp(A_w) - 1} \right], \quad (19)$$

$$J_n = F_n \left[C_p + \frac{C_p - C_n}{\exp(A_n) - 1} \right], \quad (20)$$

$$J_s = F_s \left[C_s + \frac{C_s - C_p}{\exp(A_s) - 1} \right], \quad (21)$$

$$J_h = F_h \left[C_p + \frac{C_p - C_h}{\exp(A_h) - 1} \right], \quad \text{and} \quad (22)$$

$$J_l = F_l \left[C_l + \frac{C_l - C_p}{\exp(A_l) - 1} \right]. \quad (23)$$

Here, $A_e = F_e/D_e$, $A_w = F_w/D_w$, $A_n = F_n/D_n$, $A_s = F_s/D_s$, $A_h = F_h/D_h$, and $A_l = F_l/D_l$, where $D_e = \mu_e/\Delta_{i+1/2}^x$, $D_w = \mu_w/\Delta_{i-1/2}^x$, $D_n = \mu_n/\Delta_{j+1/2}^y$, $D_s = \mu_s/\Delta_{j-1/2}^y$, $D_h = \mu_h/\Delta_{k+1/2}^z$, and $D_l = \mu_l/\Delta_{k-1/2}^z$. The J terms are conserved in each direction (Patankar 1980); that is,

$$J_e = J_w, J_n = J_s, \quad \text{and} \quad J_h = J_l. \quad (24)$$

Using (18)–(24), (17) can be rewritten as

$$\begin{aligned} \frac{(\rho C)_P^{n+1} - (\rho C)_P^n}{\Delta t} \Delta_i^x \Delta_j^y \Delta_k^z \\ + [(C_p - C_e)a_e - (C_w - C_p)a_w] \Delta_j^y \Delta_k^z \end{aligned}$$

$$\begin{aligned}
& + [(C_p - C_N)a_N - (C_S - C_P)a_S]\Delta_i^x\Delta_k^z \\
& + [(C_p - C_H)a_H - (C_L - C_P)a_L]\Delta_i^x\Delta_j^y \\
& = S_p\Delta_i^x\Delta_j^y\Delta_k^z,
\end{aligned} \quad (25)$$

where

$$\begin{aligned}
a_E &= \frac{F_e}{\exp(A_e) - 1}, & a_W &= \frac{F_w \exp(A_w)}{\exp(A_w) - 1}, \\
a_N &= \frac{F_n}{\exp(A_n) - 1}, & a_S &= \frac{F_s \exp(A_s)}{\exp(A_s) - 1}, \\
a_H &= \frac{F_h}{\exp(A_h) - 1}, & \text{and } a_L &= \frac{F_l \exp(A_l)}{\exp(A_l) - 1}.
\end{aligned} \quad (26)$$

Rearranging (25) yields

$$\begin{aligned}
C_p^{n+1} &= \frac{1}{A_p} \left(A_E C_E + A_W C_W + A_N C_N + A_S C_S + A_H C_H \right. \\
& \quad \left. + A_L C_L + \frac{\rho_p^n C_p^n}{\Delta t} + S_p \Delta_i^x \Delta_j^y \Delta_k^z \right),
\end{aligned} \quad (27)$$

where $A_E = a_E \Delta_j^y \Delta_k^z$, $A_W = a_W \Delta_j^y \Delta_k^z$, $A_N = a_N \Delta_i^x \Delta_k^z$, $A_S = a_S \Delta_i^x \Delta_k^z$, $A_H = a_H \Delta_i^x \Delta_j^y$, and $A_L = a_L \Delta_i^x \Delta_j^y$. Here, A_p is given by

$$A_p = \frac{\rho_p^{n+1}}{\Delta t} \Delta_i^x \Delta_j^y \Delta_k^z + A_E + A_W + A_N + A_S + A_H + A_L. \quad (28)$$

The linear system (27) is solved using the successive overrelaxation method. Following Versteeg and Malalasekera (1995), a nonuniform grid system is implemented in the model.

3. Simulation results and discussion

The geometrical configuration of buildings in an urban area is typically complex, with various building shapes and sizes and different spacings between buildings. Moreover, meteorological conditions change with time, with varying wind speed, wind direction, and incoming solar radiation. These factors can significantly affect flow and pollutant dispersion. To test the CFD model described in section 2 and to understand basic fluid dynamics associated with urban street-canyon flow and dispersion, three building configurations are considered in numerical simulations (Fig. 2).

In all three canonical cases, the domain size is 50 m in the x direction, 80 m in the y direction, and 50 m in the z direction. The grid interval is 1 m in both x and z directions and is 2 m in the y direction. The time step used is 0.1 s. This small time step is not essential for numerical stability because the time-differencing scheme is implicit, but it is used to resolve small-scale fluctuations in time well. The numerical model is integrated up to $t = 20$ min. Passive pollutant is continuously released at a street-level point or line source

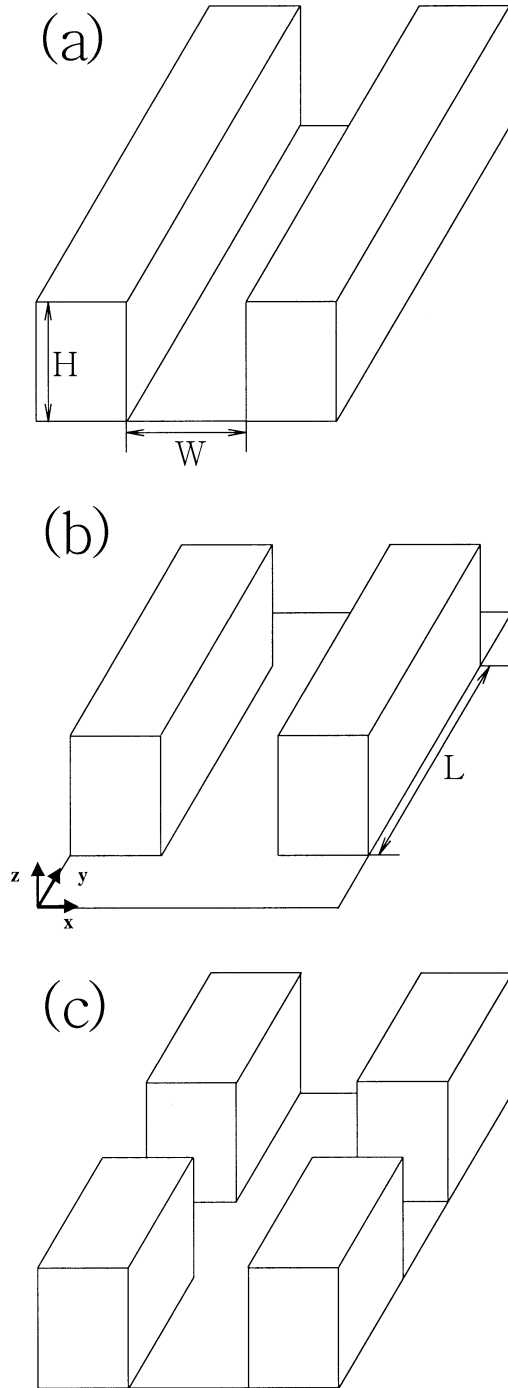


FIG. 2. (a)–(c) Three configurations of buildings in numerical simulations. Notice that in all cases the ambient wind blows from left to right in the x (streamwise) direction. The coordinate system is marked in (b).

starting from $t = 10$ min. All simulation results presented below are at $t = 20$ min, at which time the mean flow has already become quasi steady. The inflow profiles of ambient wind and turbulent kinetic energy and its dissipation rate are specified as

$$U_0 = 2.5 \left(\frac{z}{10} \right)^{0.299}, \quad (29)$$

$$k_0 = 0.005 U_0^2, \quad \text{and} \quad (30)$$

$$\varepsilon_0 = \frac{C_{\mu}^{3/4} k_0^{3/2}}{\kappa_v z}, \quad (31)$$

where U_0 is in meters per second, z is in meters, and κ_v is the von Kármán constant ($=0.4$). Notice that (29)–(31) are applied to inflow boundary. The power-law wind profile is used because it roughly imitates wind profiles near the surface (e.g., Zajic et al. 2002). The power-law profile (29) gives inflow wind speeds of 3.1 m s^{-1} at $z = 20 \text{ m}$ and 4.0 m s^{-1} at the model-top height ($z = 50 \text{ m}$). In (30), the inflow turbulent kinetic energy is specified as 1% of the inflow mean kinetic energy. No-slip conditions are applied at the solid surface, and zero-gradient conditions are applied at the outflow, spanwise, and upper boundaries. The thermal effects on flow and pollutant dispersion are examined for building configuration I only (Fig. 2a).

a. Building configuration I

This case, depicted in Fig. 2a, mimics an infinitely long canyon perpendicular to the ambient wind direction. For the simulation of flow and dispersion, the building height H and the width between the two buildings W are both set equal to 20 m . This value gives a street aspect ratio (H/W) of 1. Because the ambient wind speed above the building-roof level ($z = 20 \text{ m}$) exceeds the threshold value for stable vortex formation suggested by DePaul and Sheih (1986) and the street aspect ratio is 1, a skimming flow regime with one stable vortex in the street canyon is expected. The length of the building is practically specified as the spanwise domain size ($=80 \text{ m}$). The Reynolds number ($\text{Re} = U_{0H}H/\nu$, where U_{0H} is the inflow wind speed at $z = H$) is 4.21×10^6 . Starting from $t = 10 \text{ min}$, passive pollutant is continuously released at $(x, z) = (24.5, 0.5 \text{ m})$ along the spanwise direction (40 grid points, a line source). The emission rate at each grid point is 10 ppm s^{-1} . For presentation purposes, the predicted pollutant concentration in units of parts per million is converted to concentration in parts per billion, which is presented as a logarithm with base 10 (Figs. 3b, 4c, 11, 13, and 14).

Figure 3 shows the simulated fields of velocity vector (U, W) and pollutant concentration on the x – z plane at $y = 40 \text{ m}$. One vortex is formed in the street canyon. The center of the canyon vortex is slightly shifted downwind and upward ($x = 27 \text{ m}$, $z = 13 \text{ m}$) from the canyon center ($x = 25 \text{ m}$, $z = 10 \text{ m}$). Because of this downwind shift, downward motion near the downwind building is stronger than upward motion near the upwind building. In the building configuration, there is no upwind edge of the upwind building. The inflow is parallel to the upwind-building top surface, and no flow separation is

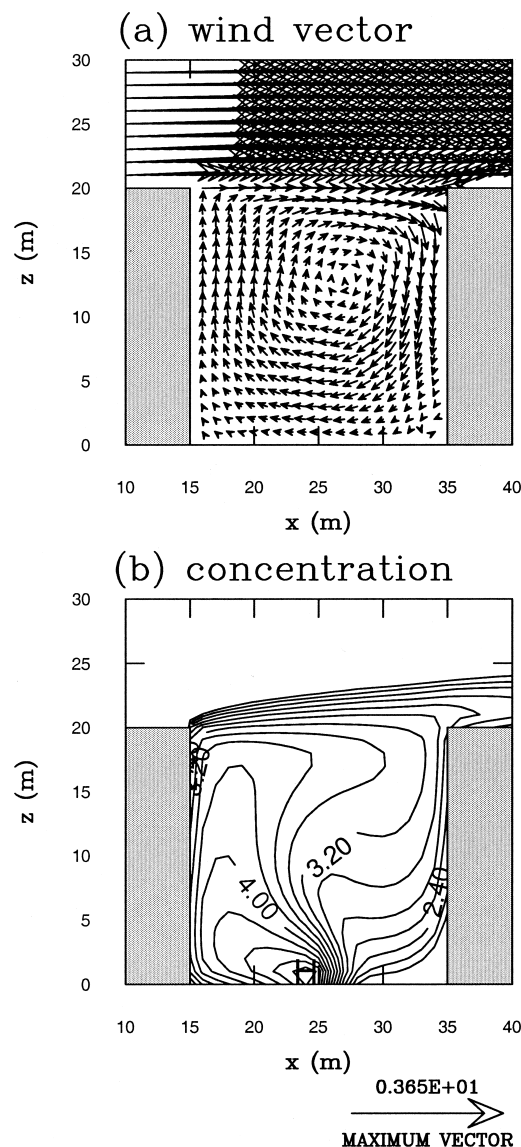


FIG. 3. Fields of (a) velocity vector (U, W) and (b) pollutant concentration on the x – z plane at $y = 40 \text{ m}$ in building configuration I. The pollutant concentration is on a logarithmic scale, and the contour interval is 0.2.

observed. However, flow separation is observed at the upwind edge of the downwind building. We found that along the spanwise direction, the velocity field on the x – z plane virtually remains the same as that in Fig. 3a. This result indicates that our CFD model successfully simulates a single roll-type vortex with a spanwise axis and spanwise homogeneity. The pollutant concentration is very high near the source location, from where pollutant is transported toward the upwind building and then upward by the vortex circulation. At any height of the street canyon, the pollutant concentration is higher near the upwind building than near the downwind building. This pattern is because highly polluted air passing through the street-level source is advected upward on

the upwind side while relatively less polluted air enters the street canyon by the downward motion on the downwind side. Considering the transverse homogeneity, in many previous modeling studies on urban street-canyon flow and dispersion (e.g., Lee and Park 1994; Sini et al. 1996; Baik and Kim 1999; Huang et al. 2000), a two-dimensional approach could be adopted.

To examine factors or processes responsible for the pollutant escape from the urban street canyon, the horizontally integrated vertical mean and turbulent fluxes at the canyon-top height ($z = 20$ m) are computed using

$$\beta_m = \int_y \int_x F_m dx dy \quad \text{and} \quad (32)$$

$$\beta_t = \int_y \int_x F_t dx dy, \quad (33)$$

respectively. Here, F_m is the vertical flux of pollutant by mean flow ($=CW$) and F_t is the vertical flux of pollutant by turbulent flow ($=\overline{cw}$), which is calculated using (7) ($\overline{cw} = -K_c \partial C / \partial z$). The integrations are performed over the canyon-top area from $x = 15$ to 35 m and from $y = 0$ to 80 m. The calculated fluxes are $\beta_m = -2.9 \text{ ppm m}^3 \text{ s}^{-1}$ and $\beta_t = 200.6 \text{ ppm m}^3 \text{ s}^{-1}$. As in two dimensions (Baik and Kim 2002), this result indicates that pollutant escapes from the street canyon mainly by turbulent processes and that the net effect of mean flow is to make some escaped pollutant reenter the street canyon. The results from two-dimensional experiments with different inflow turbulence intensities, wind speeds, and street aspect ratios, as well as from the case of two isolated buildings, are discussed in Baik and Kim (2002); all of their simulation results show that turbulent processes are mainly responsible for the pollutant escape from urban street canyons.

In the current CFD model, the standard k - ϵ turbulence model is employed. This standard model is known to overestimate turbulent kinetic energy, particularly in the region close to the building edge (we plan to improve this standard model in the near future). Therefore, the vertical turbulent flux of pollutant in the region close to the downwind building edge may not be very reliable. However, our concern here is the horizontally integrated turbulent flux of pollutant at the canyon-top height in order to examine the mechanism responsible for pollutant escape from the street canyon. Hence, considering that the vertical turbulent flux of pollutant near the downwind building at the canyon-top height is relatively small as compared with that at other regions [see Baik and Kim (2002) for detailed analysis in two dimensions], the calculated value of the integrated vertical turbulent flux appears to be reasonable.

During the daytime, the street bottom and building surface are heated by incoming solar radiation. An observational study by Nakamura and Oke (1988) shows that the maximum temperature difference between the building surface and the air can be as large as 12° – 14°C .

A wind-tunnel study by Uehara et al. (2000) and two-dimensional modeling studies by Sini et al. (1996) and Kim and Baik (1999, 2001) indicate that the heating can significantly affect flow and dispersion in urban street canyons. To delve into such phenomena using the three-dimensional CFD model, the effects of street-bottom heating are examined. For this, the initial air temperature is specified as 20°C and the street bottom remains at a fixed temperature of 25°C . A wall function is derived and is used to represent the heat transfer between the street bottom and the air (Abadie and Schiestel 1986; Ciofalo and Collins 1989).

Figure 4 shows the fields of velocity vector (U , W), temperature, and pollutant concentration on the x - z plane at $y = 40$ m in the presence of street-bottom heating. One vortex is formed in the canyon. The center of the vortex here is located closer to the canyon center, and the vortex is stronger than that in the case without bottom heating (Fig. 3a). The strengthened vortex is clearly seen in the vertical profiles of vertical velocity at upwind and downwind locations (Fig. 5). When there is street-bottom heating, the vertical axis connecting maximum temperature points at any height of the lower canyon is located near the upwind building (Fig. 4b). This results from the fact that the maximum temperature axis is advected toward the upwind building by the lower vortex circulation. Therefore, because of the positive buoyancy, upward motion is thermally induced near the upwind building and the resulting motion is constructively combined with mechanically induced upward motion to strengthen upward motion near the upwind building. By mass conservation, the horizontal flow toward the upwind building in the lower canyon intensifies. In accord, the downward flow near the downwind building and the horizontal flow toward the downwind building in the upper canyon also intensify. This process results in a stronger vortex in the canyon. To examine the strength of the vortex in the canyon with and without bottom heating in terms of vorticity, the vorticity in the y direction was calculated. As expected, the positive vorticity near the canyon center was enhanced when there was bottom heating (figure not shown).

When there is bottom heating, turbulent mixing increases and, thus, the gradient of pollutant concentration in the street canyon decreases (cf. Fig. 3b and Fig. 4c). On the downwind side of the canyon, the pollutant concentration is higher with bottom heating than without bottom heating.

As was done with the two-dimensional model (Baik and Kim 2002), the developed three-dimensional CFD model is validated against the fluid experimental data. The mean velocity data obtained from the physical experiment using a circulating water channel (Odell and Kovaszny 1971; Baik et al. 2000) are used to compare mean flows (Baik and Kim 2002). Figure 6 shows the vertical profiles of normalized vertical velocity at a downwind location ($x_d/W = 0.85$) of the model street canyon at the middle of spanwise domain in the cir-

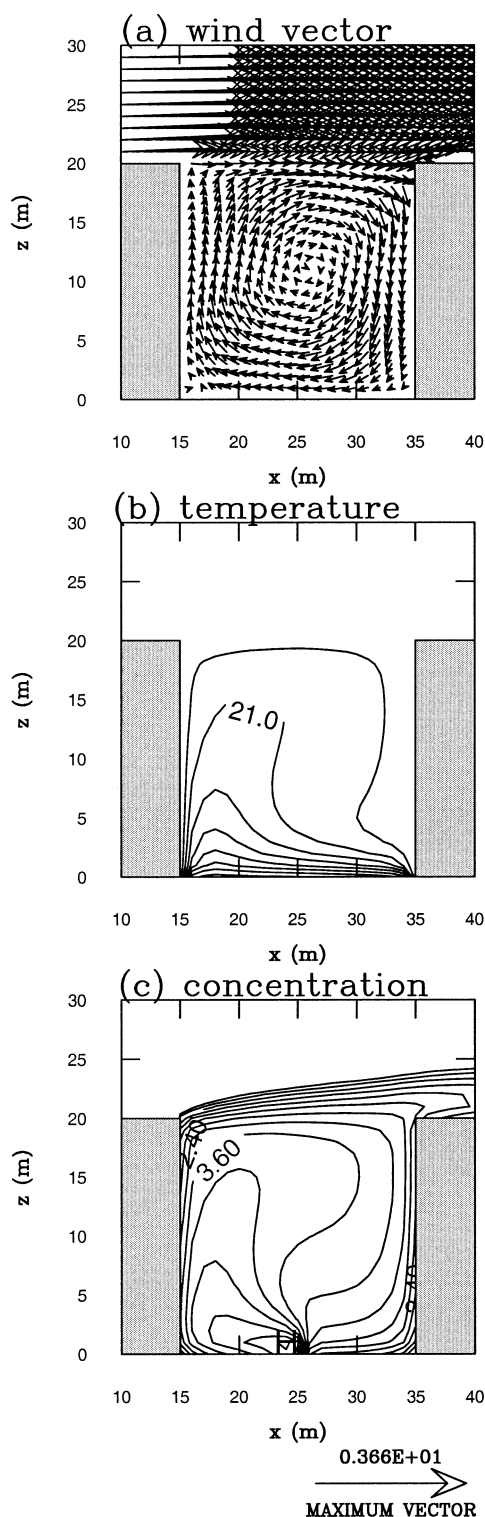


FIG. 4. Fields of (a) velocity vector (U , W), (b) temperature, and (c) pollutant concentration on the x - z plane at $y = 40$ m in building configuration I with street-bottom heating. The pollutant concentration is on a logarithmic scale. The contour intervals in (b) and (c) are 0.5°C and 0.2 .

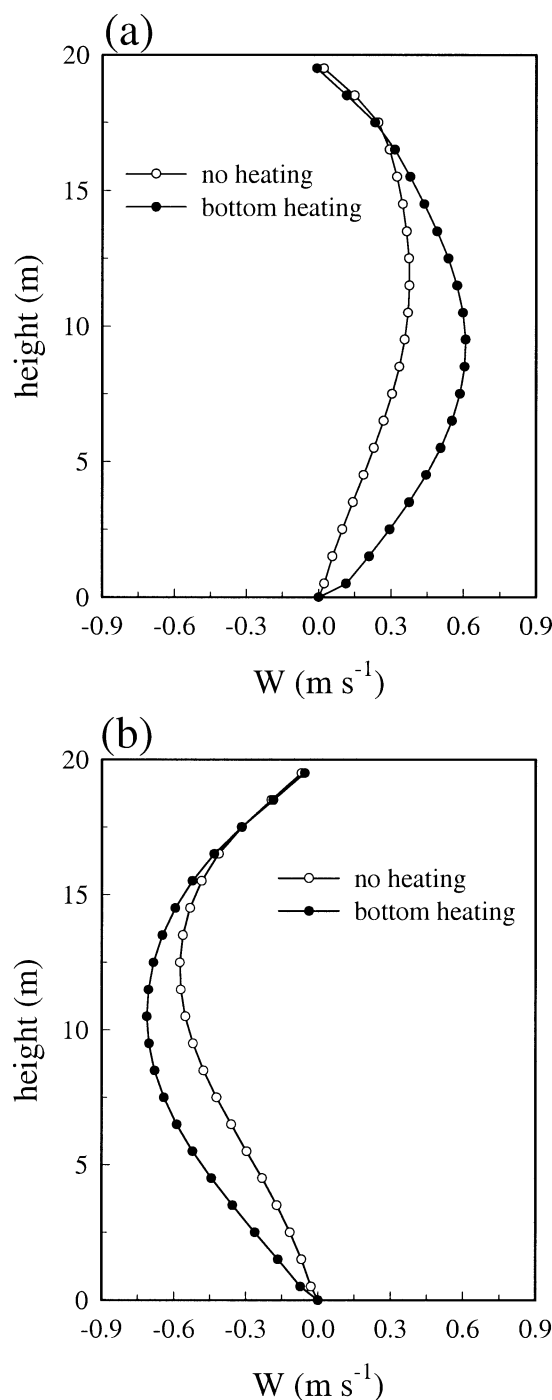


FIG. 5. Vertical profiles of vertical velocity at locations of (a) $(x, y) = (18, 40)$ m and (b) $(32, 40)$ m in building configuration I with and without street-bottom heating.

culating-water-channel experiment and numerical experiment (no bottom-heating case). The normalized downward velocity near $z/H = 0.9$ is stronger in the numerical experiment than in the water-channel experiment, but as a whole the two vertical profiles of normalized vertical velocity are similar to each other.

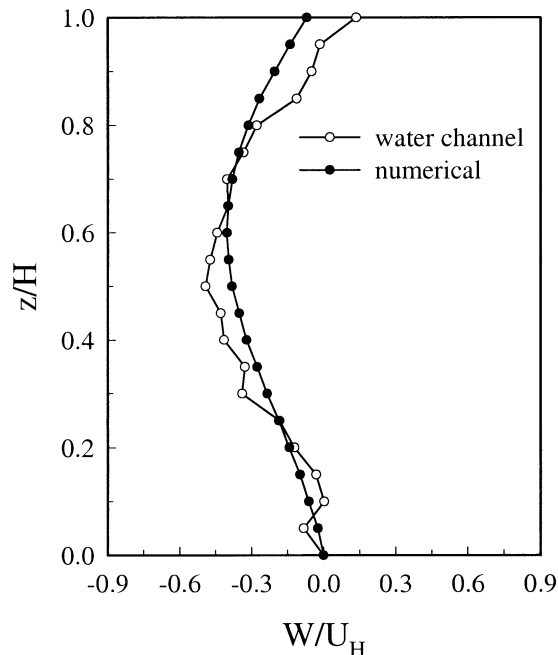


FIG. 6. Vertical profiles of normalized vertical velocity at a downwind location ($x_d/W = 0.85$, where x_d is the horizontal distance from the upwind building corner) of the model street canyon at the middle of spanwise domain in the circulating water channel (Baik and Kim 2002) and numerical (building configuration I case without bottom heating) experiments. The height is normalized by the model building height H , and the vertical velocity is normalized by the horizontal velocity U_H averaged across the top of the street canyon.

The data for the urban roughness case obtained through a wind-tunnel experiment (Meroney et al. 1996) are used to compare pollutant concentrations. Figure 7 shows normalized pollutant concentrations at 11 locations in the wind-tunnel experiment versus corresponding ones in the numerical experiment (no bottom-heating case). The pollutant concentration is normalized by the concentration at location 7 (face of the upwind building at $z/H = 0.17$), where the highest concentration is observed among the selected 11 locations. The three locations (measurement locations 1–3) in Meroney et al. (1996) are not included in this figure. The flow above the upwind model building is parallel to the bottom and, in accord, pollutant insignificantly penetrates into the region just above the upwind building because a reversed flow is absent there. The normalized pollutant concentration in the numerical experiment tends to be lower than that in the wind-tunnel experiment. Despite this tendency, the degree of a linear fitting is good ($R^2 = 0.80$).

The present CFD model was further validated against the data obtained through a wind-tunnel experiment with bottom heating (Uehara et al. 2000). In the numerical simulation, the initial air temperature is 20°C and the temperature at the street bottom is fixed at 22°C. The computed bulk Richardson number is -0.27 . For comparison, the vertical profile of normalized horizontal ve-

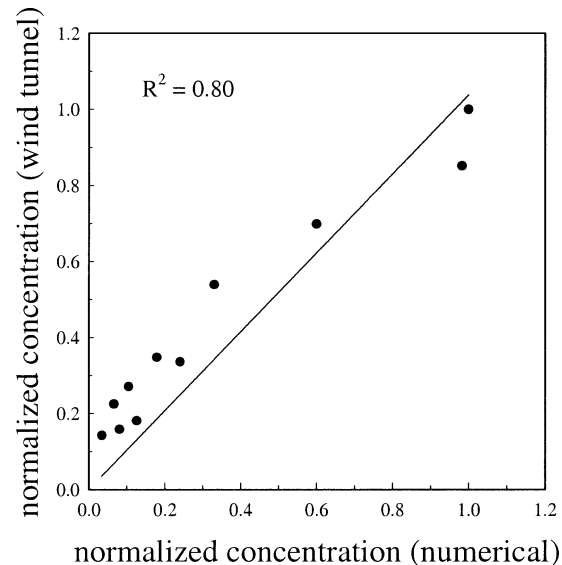


FIG. 7. Normalized pollutant concentrations at 11 locations in the wind-tunnel experiment (Meroney et al. 1996) vs corresponding normalized pollutant concentrations in the numerical experiment (building configuration I case without bottom heating). For the 11 locations, see Baik and Kim (2002). The pollutant concentration is normalized by its value at location 7.

locity at the center of the street canyon in the numerical simulation was compared with that in the wind-tunnel experiment with a bulk Richardson number of -0.21 . The degree of linear fitting between the two datasets was very good, with $R^2 = 0.92$. Good agreement between the numerical and fluid experiments (Fig. 6, Fig. 7, and the comparison result in the presence of bottom heating) supports the physical realization of the developed three-dimensional CFD model.

b. Building configuration II

In this case (Fig. 2b), the building length is finite and the ambient wind blows perpendicular to the street canyon. The building height H , width between the two buildings W , and building length L are specified as 20, 20, and 40 m, respectively. Thus, $H/W = 1$ and $H/L = 0.5$. This canyon geometry is expected to give a skimming flow regime in the canyon [see Fig. 2 of Hunter et al. (1992)]. Passive pollutant is released at a location of $(x, y, z) = (24.5, 39, 0.5)$ m, a point source very close to the center of the street bottom $(x, y, z) = (25, 40, 0)$ m. Notice that the grid system is staggered. The emission rate is 400 ppm s^{-1} at the grid point.

A series of two-dimensional cross sections of the flow are analyzed to examine the three-dimensional structure of the flow formed in the street canyon. Figure 8 shows horizontal velocity vector field (U, V) on the x - y plane at $z = 2, 10$, and 18 m. On the midcanyon plane (Fig. 8b), double-vortex (or double eddy) circulation appears, which is confined within the street canyon. As flow separates near the corners of the upwind building, lower-

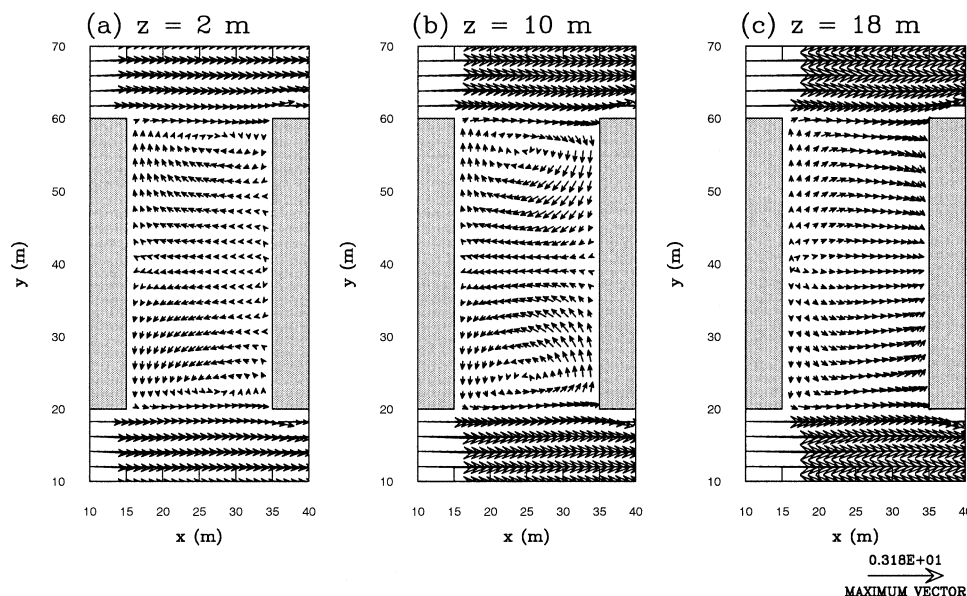


FIG. 8. Velocity vector (U , V) field on the x - y plane at $z =$ (a) 2, (b) 10, and (c) 18 m in building configuration II.

pressure regions are created at the sides and in the lee of the upwind building (Hunter et al. 1992), leading to the observed double-vortex circulation. In each vortex, the horizontal velocity is stronger near the downwind building than near the upwind building. If the street width W becomes wider and wider, the transition from skimming to wake interference and then to isolated roughness flow regime occurs. In isolated roughness flow regime, beyond double-vortex circulation, the flow is characterized by a relatively strong streamwise velocity component (Hunter et al. 1992). At $z = 2$ m (Fig. 8a), the double-vortex circulation also appears, but its intensity is weaker than that on the midcanyon plane. In each vortex, the horizontal velocity is stronger near the upwind building than near the downwind building. This relatively stronger horizontal velocity contributes to the transport of pollutant outward from the canyon center region (see Fig. 11a). Close to the canyon-top height, the horizontal flow is mainly directed in the streamwise direction (Fig. 8c) because of the influence of the ambient wind. The flow field at each height in Fig. 8 is symmetric about $y = 40$ m, indicating that the three-dimensional CFD model simulates the symmetry of the flow configuration very well.

Figure 9 shows velocity vector field (U , W) on the x - z plane at $y = 30$, 40, and 50 m. The flow pattern is similar to that in the case with an infinitely long canyon perpendicular to the ambient wind direction (Fig. 3a, building configuration I). As the building length becomes longer, a region having the characteristics of the street-canyon flow that corresponds to building configuration I becomes wider in spanwise extent. When the building length is much larger than the width between buildings, simulated urban street-canyon flow will be

essentially the flow in an infinitely long canyon perpendicular to the ambient wind direction, except near the ends of the canyon where the flow pattern similar to that described on the half plane in Fig. 8 will appear.

Figure 10 shows velocity vector field (V , W) on the y - z plane at $x = 18$, 25, and 32 m. Near the upwind building (Fig. 10a), the canyon flow is directed outward and upward. Near the street bottom, the magnitude of the spanwise component of velocity is larger than that of the vertical component. This spanwise component of velocity plays an important role in transporting pollutant outward along near the upwind building (Fig. 11a). Near the downwind building (Fig. 10c), the canyon flow is directed inward and downward and brings in less polluted air. At $x = 25$ m (Fig. 10b), the flow is relatively weak. On each half plane of the canyon, the spanwise inward flow is observed around $z = 13$ m, and this flow diverges upward and downward near the canyon center. These flow patterns can be considered as a combined flow of the two-dimensional vortex formed in the street canyon (Fig. 9) and the horizontal double-vortex circulation (Fig. 8). For example, at $(y, z) = (43, 10)$ m on the plane at $x = 18$ m (Fig. 10a), the two-dimensional vortex gives upward motion and the double-eddy circulation gives outward horizontal motion, yielding outward and upward components of velocity at the point.

The pollutant concentration field at each height corresponding to Fig. 8 is presented in Fig. 11. At $z = 2$ m (Fig. 11a), the pollutant concentration is very high near the source. Along any streamwise line, the pollutant concentration is much higher near the upwind building than near the downwind building. Pollutant near the source is transported toward the upwind building and then laterally and upward. The lateral spreading is fa-

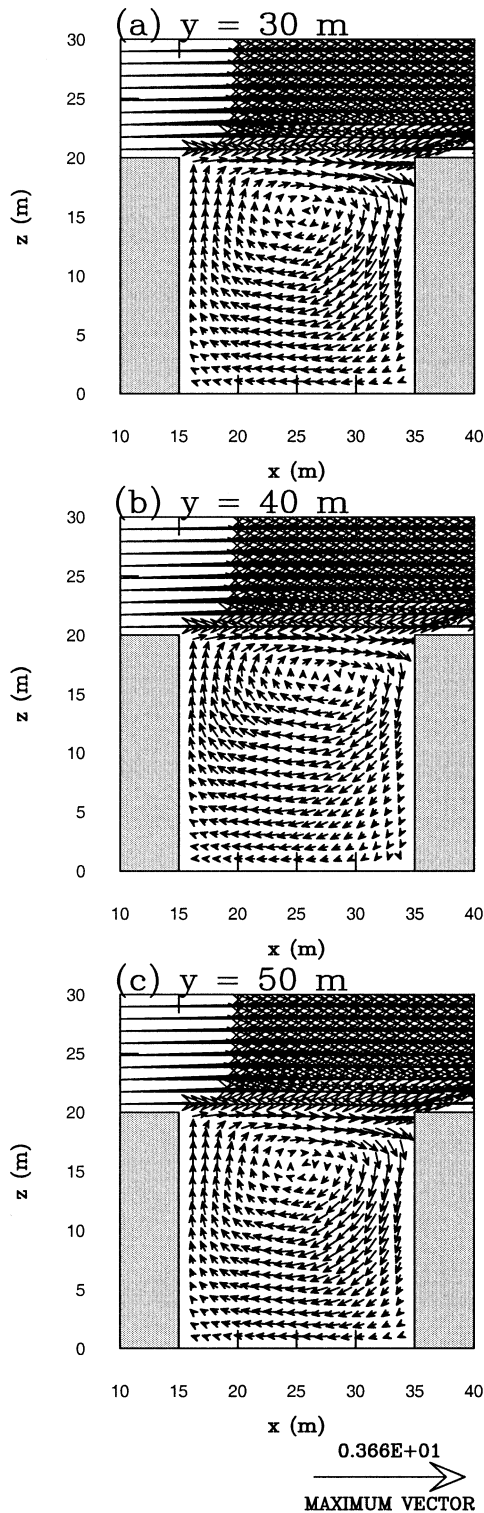


FIG. 9. Velocity vector (U , W) field on the x - z plane at $y =$ (a) 30, (b) 40, and (c) 50 m in building configuration II.

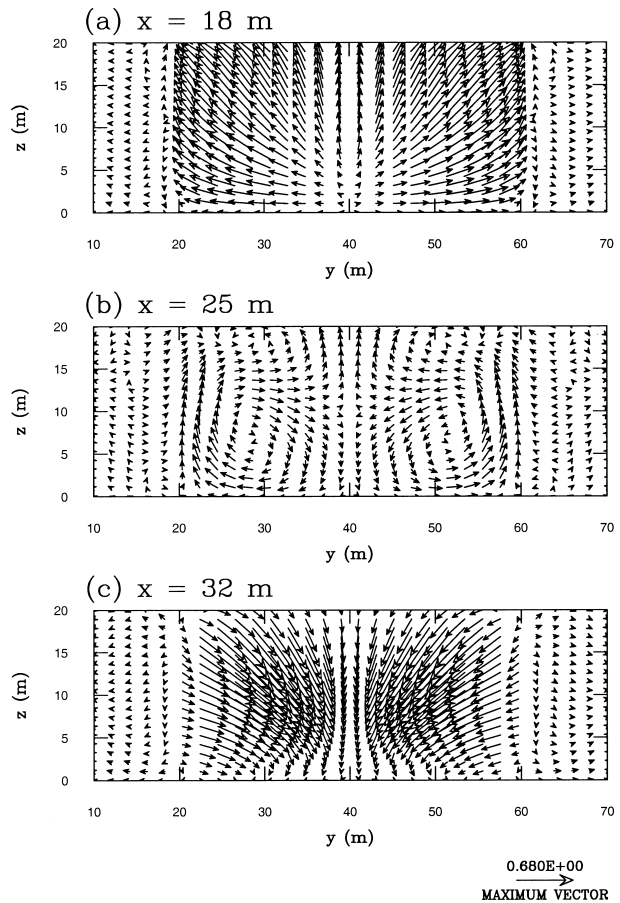


FIG. 10. Velocity vector (V , W) field on the y - z plane at $x =$ (a) 18, (b) 25, and (c) 32 m in building configuration II.

cilitated by the horizontal flow in the region close to the street bottom (Fig. 10a). At $z = 10$ m (Fig. 11b), the pollutant concentration is highest near the center of the upwind building. This pattern is because highly polluted air is transported from below by the upward motion (Fig. 9b). At $z = 18$ m, the highest pollutant concentration is observed near the center of the upwind building. Because the point source is located at $(x, y, z) = (24.5, 39, 0.5)$ m, the pollutant concentration at any point in the canyon with $y < 40$ m is higher than that at its image location about the plane at $y = 40$ m.

In building configuration II, processes responsible for the pollutant escape from the street canyon can be examined by calculating the mean and turbulent fluxes of pollutant. The horizontally integrated vertical mean and turbulent fluxes over the canyon-top area, that is, an area from $x = 15$ to 35 m and from $y = 20$ to 60 m at $z = 20$ m, are $\beta_m = 4.5 \text{ ppm m}^3 \text{ s}^{-1}$ and $\beta_t = 59.5 \text{ ppm m}^3 \text{ s}^{-1}$, respectively. The integrated horizontal mean and turbulent fluxes over one canyon-end area from $x = 15$ to 35 m and from $z = 0$ to 20 m at $y = 20$ m are $\beta_m = 2.6 \text{ ppm m}^3 \text{ s}^{-1}$ and $\beta_t = -98.4 \text{ ppm m}^3 \text{ s}^{-1}$. For this canyon-end area, positive (negative) flux value means that pollutant grossly reenters (escapes

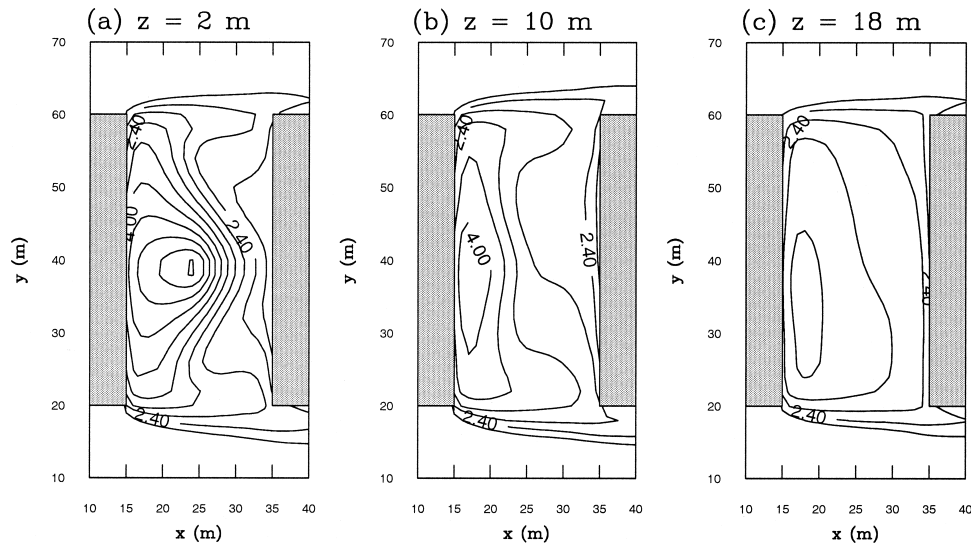


FIG. 11. Pollutant concentration field on the x - y plane at $z =$ (a) 2, (b) 10, and (c) 18 m in building configuration II. The pollutant concentration is on a logarithmic scale, and the contour interval is 0.4.

from) the canyon. The horizontal mean and turbulent fluxes integrated over the other canyon-end area, that is, from $x = 15$ to 35 m and from $z = 0$ to 20 m at $y = 60$ m, are $\beta_m = -1.0 \text{ ppm m}^3 \text{ s}^{-1}$ and $\beta_t = 36.4 \text{ ppm m}^3 \text{ s}^{-1}$. For this canyon-end area, positive (negative) flux value means that pollutant grossly escapes from (reenters) the canyon. Therefore, similar to building configuration I, turbulent processes are mainly responsible for the pollutant escape from the street canyon.

c. Building configuration III

The third building configuration is a case with orthogonally intersecting canyons (Fig. 2c). The ambient wind blows in the x direction. The building height H , street width W , and truncated building length L are specified as 20, 20, and 30 m, respectively. Passive pollutant is released at a location of $(x, y, z) = (9.5, 39, 0.5)$ m with an emission rate of 400 ppm s^{-1} .

Figure 12 shows horizontal velocity vector field at $z = 2, 10$, and 18 m. The flow in the street canyon between

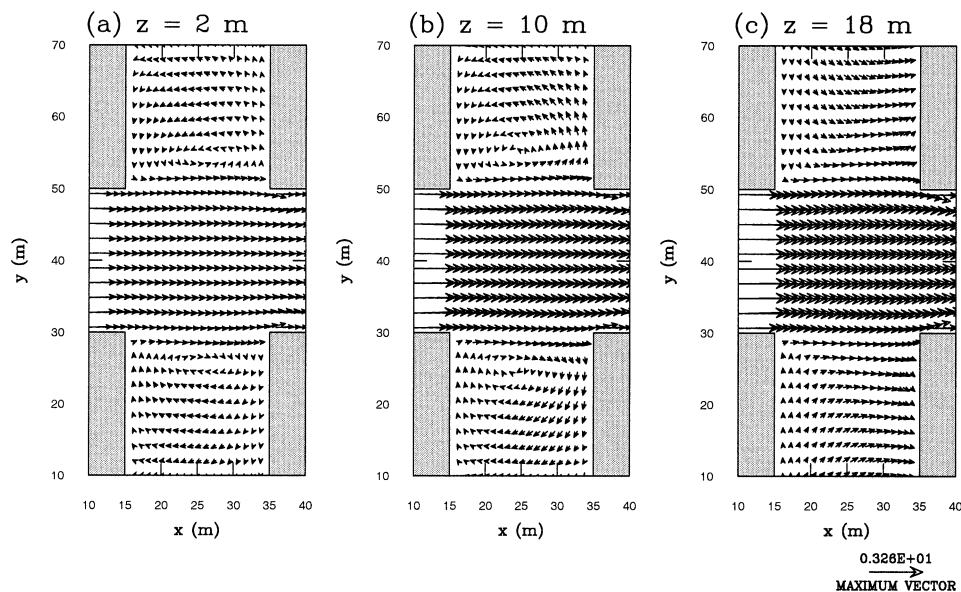


FIG. 12. Velocity vector (U, V) field on the x - y plane at $z =$ (a) 2, (b) 10, and (c) 18 m in building configuration III.

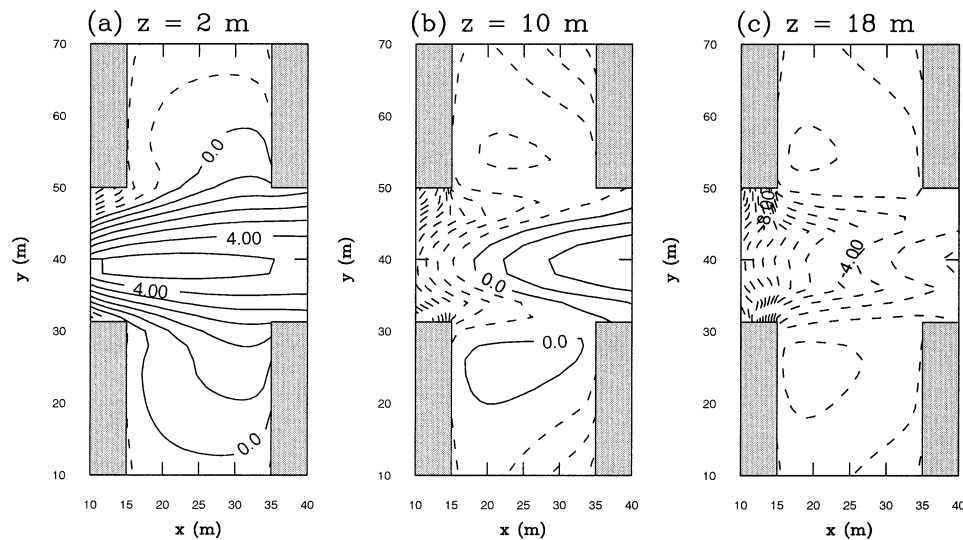


FIG. 13. Pollutant concentration field on the x - y plane at $z =$ (a) 2, (b) 10, and (c) 18 m in building configuration III. The pollutant concentration is on a logarithmic scale, and the contour interval is 0.8.

$y = 30$ and 50 m is essentially the ambient flow. The circulation formed in the street canyon of $x = 15$ – 35 m and $y = 0$ – 30 m (also $x = 15$ – 35 m and $y = 50$ – 80 m) resembles circulation on the half plane of the canyon in building configuration II (Fig. 8b).

The pollutant concentration field at $z = 2$, 10, and 18 m is presented in Fig. 13. At $z = 2$ m, pollutant is mainly transported in the streamwise direction in the street canyon between $y = 30$ and 50 m. The lateral decrease of pollutant concentration from the line at $y = 40$ m is evident, with its gradient being higher in the spanwise direction than in the streamwise direction. In the street canyon of $x = 15$ – 35 m and $y = 0$ – 30 m (also

$x = 15$ – 35 m and $y = 50$ – 80 m), pollutant enters the canyon mainly by turbulent transport. The pollutant concentration is relatively high near the inside region of the corner of each upwind building. At $z = 10$ m, the high pollutant concentration region is located farther downwind in the streamwise direction because of the pollutant transport by the ambient wind. The high pollutant concentration region is shifted farther downwind at $z = 18$ m. Each concentration field in Fig. 13 is not symmetric about $y = 40$ m because of the source location of $y = 39$ m. A numerical experiment is conducted in which passive pollutant is released at two locations: $(x, y, z) = (9.5, 39, 0.5)$ m and $(9.5, 41, 0.5)$ m. The emission rate at each point is 200 ppm s^{-1} . In this case, the CFD model produces the expected symmetric pattern of concentration field about $y = 40$ m (Fig. 14).

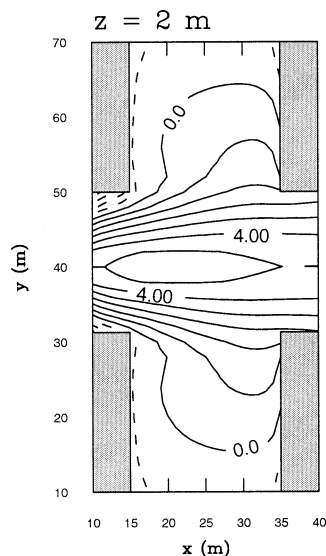


FIG. 14. Same as in Fig. 13a, except that passive pollutant is released at two locations: $(x, y, z) = (9.5, 39, 0.5)$ m and $(9.5, 41, 0.5)$ m, with an emission rate of 200 ppm s^{-1} at each point.

4. Summary and conclusions

A three-dimensional computational fluid dynamics model was developed for urban flow and dispersion research. The model equations are the Reynolds-averaged momentum, mass continuity, heat, and passive pollutant equations under the Boussinesq approximation. The Reynolds stresses and turbulent fluxes are parameterized using the eddy diffusivity approach. The turbulent diffusivities of momentum, heat, and pollutant concentration are calculated with the prognostic equations of turbulent kinetic energy and its dissipation rate. The model employs a staggered, nonuniform grid system. The governing equation set is solved numerically using a finite-volume method with the SIMPLE algorithm. The CFD model was tested by simulating urban street-canyon flow and pollutant dispersion. Three different building configurations were considered: infinitely long canyon, long canyon of finite length, and orthogonally inter-

secting canyons. Passive pollutant was released at a street-level point or line source. Analysis of simulation results indicated that the model is capable of simulating urban street-canyon flow and pollutant dispersion reasonably well.

Recent physical experiments (e.g., Brown et al. 2001) have provided high-resolution data on the mean velocity and turbulence statistics around a model-building cluster in a wind tunnel. Recent field experiments (e.g., Zajic et al. 2002) have also provided invaluable data on the mean velocity and turbulence statistics around a building cluster. The CFD model presented in this study can be more rigorously tested and improved in the near future using available data. In modeling urban flow and dispersion, smaller grid sizes are desirable near buildings to resolve flow and dispersion fields better there, but away from buildings larger grid sizes are allowable. To make the CFD model efficient for a given computing resource, a nonuniform grid system is implemented in the current model, although the simulations presented in this study were performed with a uniform grid system. The CFD model with a nonuniform grid system will be rigorously tested in the near future. With ever-increasing computing power, this CFD model can be used to simulate flow and pollutant dispersion in a real urban area with a cluster of buildings. In these simulations, boundary conditions for the CFD model can be provided using observed meteorological data or the forecasts of a mesoscale numerical model with fine horizontal and vertical resolutions. This will be a topic of our future research.

Acknowledgments. The authors thank two anonymous reviewers for providing valuable comments on this study. The first author (JJB) was supported by the Climate Environment System Research Center sponsored by the SRC Program of the Korea Science and Engineering Foundation and also by the Brain Korea 21 Project. The second (JJK) and third (HJSF) authors were supported, in part, by the U.S. Army Research Office.

REFERENCES

- Abadie, P., and R. Schiestel, 1986: Prevision numérique de la convection forcée turbulente dans une cavité bidimensionnelle entrainée. *Int. J. Heat Mass Transfer*, **29**, 417–427.
- Arya, S. P., 1999: *Air Pollution Meteorology and Dispersion*. Oxford University Press, 310 pp.
- Baik, J.-J., and J.-J. Kim, 1999: A numerical study of flow and pollutant dispersion characteristics in urban street canyons. *J. Appl. Meteor.*, **38**, 1576–1589.
- , and —, 2002: On the escape of pollutants from urban street canyons. *Atmos. Environ.*, **36**, 527–536.
- , R.-S. Park, H.-Y. Chun, and J.-J. Kim, 2000: A laboratory model of urban street-canyon flows. *J. Appl. Meteor.*, **39**, 1592–1600.
- Brown, M. J., R. E. Lawson, D. S. DeCroix, and R. L. Lee, 2001: Comparison of centerline velocity measurements obtained around 2D and 3D building arrays in a wind tunnel. *Third Int. Symp. on Environmental Hydraulics*, Tempe, AZ, The University of Hong Kong, 114.
- Ciofalo, M., and M. W. Collins, 1989: k - ϵ predictions of heat transfer in turbulent recirculating flows using an improved wall treatment. *Numer. Heat Transfer*, **15B**, 21–47.
- DePaul, F. T., and C. M. Sheih, 1985: A tracer study of dispersion in an urban street canyon. *Atmos. Environ.*, **19**, 555–559.
- , and —, 1986: Measurements of wind velocities in a street canyon. *Atmos. Environ.*, **20**, 455–459.
- Hoydys, W. G., and W. F. Dabberdt, 1988: Kinematics and dispersion characteristics of flows in asymmetric street canyons. *Atmos. Environ.*, **22**, 2677–2689.
- Huang, H., Y. Akutsu, M. Arai, and M. Tamura, 2000: A two-dimensional air quality model in an urban street canyon: Evaluation and sensitivity analysis. *Atmos. Environ.*, **34**, 689–698.
- Hunter, L. J., G. T. Johnson, and I. D. Watson, 1992: An investigation of three-dimensional characteristics of flow regimes within the urban canyon. *Atmos. Environ.*, **26B**, 425–432.
- Kim, J.-J., and J.-J. Baik, 1999: A numerical study of thermal effects on flow and pollutant dispersion in urban street canyons. *J. Appl. Meteor.*, **38**, 1249–1261.
- , and —, 2001: Urban street-canyon flows with bottom heating. *Atmos. Environ.*, **35**, 3395–3404.
- Lee, I. Y., and H. M. Park, 1994: Parameterization of the pollutant transport and dispersion in urban street canyons. *Atmos. Environ.*, **28**, 2343–2349.
- Lee, R. L., R. J. Calhoun, S. T. Chan, J. Leone Jr., and D. E. Stevens, 2001: Modeling of building scale flow and dispersion. *Third Int. Symp. on Environmental Hydraulics*, Tempe, AZ, The University of Hong Kong, 119.
- Meroney, R. N., M. Pavageau, S. Rafailidis, and M. Schatzmann, 1996: Study of line source characteristics for 2-D physical modeling of pollutant dispersion in street canyons. *J. Wind Eng. Ind. Aerodyn.*, **62**, 37–56.
- Nakamura, Y., and T. R. Oke, 1988: Wind, temperature, and stability conditions in an east-west oriented urban canyon. *Atmos. Environ.*, **22**, 2691–2700.
- Odell, G. M., and L. S. G. Kovaszny, 1971: A new type of water channel with density stratification. *J. Fluid. Mech.*, **50**, 535–543.
- Patankar, S. V., 1980: *Numerical Heat Transfer and Fluid Flow*. McGraw-Hill, 197 pp.
- Raupach, M. R., R. A. Antonia, and S. Rajagopalan, 1991: Rough-wall turbulent boundary layers. *Appl. Mech. Rev.*, **44**, 1–25.
- Rotach, M. W., 1995: Profiles of turbulence statistics in and above an urban street canyon. *Atmos. Environ.*, **29**, 1473–1486.
- Roth, M., 2000: Review of atmospheric turbulence over cities. *Quart. J. Roy. Meteor. Soc.*, **126**, 941–990.
- Sini, J.-F., S. Anquetin, and P. G. Mestayer, 1996: Pollutant dispersion and thermal effects in urban street canyons. *Atmos. Environ.*, **30**, 2659–2677.
- Uehara, K., S. Murakami, S. Oikawa, and S. Wakamatsu, 2000: Wind tunnel experiments on how thermal stratification affects flow in and above urban street canyons. *Atmos. Environ.*, **34**, 1553–1562.
- Versteeg, H. K., and W. Malalasekera, 1995: *An Introduction to Computational Fluid Dynamics: The Finite Volume Method*. Longman, 257 pp.
- Zajic, D., M. Princevac, J.-J. Kim, H. J. S. Fernando, and J.-J. Baik, 2002: Flow and turbulence surrounding a building cluster. *Fourth Symp. on Urban Environment*, Norfolk, VA, Amer. Meteor. Soc., J32–J33.
- Zhang, Y. Q., S. P. Arya, and W. H. Snyder, 1996: A comparison of numerical and physical modeling of stable atmospheric flow and dispersion around a cubical building. *Atmos. Environ.*, **30**, 1327–1345.